Int J Adv Manuf Technol
DOI 10.1007/s00170-011-3890-5

ORIGINAL ARTICLE

Weldability and joining characteristics of AISI 430/AISI 1040 steels using keyhole plasma arc welding

Tanju Teker · Niyazi Özdemir

Received: 17 October 2011 / Accepted: 28 December 2011

Abstract AISI 430 and AISI 1040 steel couples were welded using the keyhole plasma-transferred arc (KPTA) welding process. Welded joints were manufactured using three different traverse speeds (0.01, 0.02 and 0.03 m/min) under three different welding currents (130, 135 and 140 A) at a constant plasma gas flow rate (1.1 l/min) and a shielding gas rate (25 l/min). In order to determine the microstructural changes that occurred, the interface regions of the welded specimens were examined by Scanning Electron Microscopy (SEM), X-ray Diffraction (XRD) and Energy Dispersive Spectrometry (EDS) after KPTA welding. Microhardness, V-notch Charpy and tensile tests were conducted to determine the mechanical properties of the welded specimens.

Keywords Keyhole welding · Microstructure · Mechanical properties

1 Introduction

Plasma-transferred arc (PTA) welding is very similar to conventional gas tungsten arc welding (GTAW) in the sense that a plasma jet is used as a source of intense heat to melt the material to be welded. When the tungsten electrode is located within the torch nozzle and the orifice, the arc is restricted and the highly constrained plasma jet can displace the molten metal in the weld pool to form a keyhole going completely through the base metal [1]. Three operating modes can be produced by varying the bore diameter and the plasma gas flow rate: microplasma operates between 0.1 and 15 A, medium plasma uses currents between 15 and 100 A and keyhole plasma operates above 100 A [2–5]. A highly powerful plasma can be produced by increasing the plasma gas flow rate and the welding current, thus enabling full penetration of the workpiece (similar to laser welding) [6]. Compared to laser beam welding and electron beam welding, keyhole plasma-transferred arc welding (KPTAW) is more cost effective and more tolerant of joint preparation, though its energy is less dense and its keyhole is wider. On the other hand, KPTAW offers significant advantages over GTAW in terms of penetration depth and thermal distortion. Thus, KPTAW has found applications on the welding of structural steels, automobiles, airplanes, rockets and space shuttles. With a proper combination of orifice gas flow, travel speed and welding current, keyhole formation is possible, allowing higher welding speeds than GTAW with full penetrations. The keyhole progressively cuts through the metal, with the molten weld pool flowing behind the hole and forming a weld bead. The keyhole process is used to weld thicker materials such as 10-mm thick stainless steel plates in one single pass [7–9]. Ferritic stainless steels, which are noted not only for their high resistance to stress corrosion cracking (SCC), pitting and crevice corrosion in chloride environments but also for their poor toughness especially in the welded condition, comprise approximately half of the 400 series stainless steels. These steels contain between 10.5 and 30 wt.% chromium along with other alloying elements, particularly molybdenum. Ideally, ferritic stainless steels have body-centered cubic (BCC) crystal structure known as ferrite at all temperatures below their

T. Teker (✉)
Vocational Education Center,
23500 Elazığ, Turkey
e-mail: tteker@hotmail.com

N. Özdemir
Department of Metal, University of Fırat,
Faculty of Technical Education,
23119 Elazığ, Turkey
e-mail: nozdemir@firat.edu.tr

Published online: 15 January 2012

Table 1 Chemical composition of test materials

Chemical composition (wt.%)										
Alloy	Fe	C	Cr	Ni	Si	Mo	S	Mn	P	Cu
AISI 430	82.64	0.048	16.02	0.22	0.44	0.016	0.002	0.610	–	–
AISI 1040	97.9	0.39	–	–	0.158	–	0.022	0.65	0.034	0.31

melting temperatures. Many of these alloys are subject to the precipitation of undesirable intermetallic phases when exposed to certain temperature ranges. Higher chromium alloys can be embrittled by the precipitation of the tetragonal sigma phase, which is based on the FeCr compound. The ability to join ferritic stainless steel both to itself and to other materials with conventional fusion welding processes such as gas tungsten, laser beam and electron beam welding opens up the possibility of producing unexpected phase propagation, and a series of negative metallurgical changes like sigma phase and grain coarsening occur in the heat-affected zone (HAZ). Therefore, extensive care and precautions such as pre- and postheat treatments or quick welding speeds are required. In practice, the process of joining dissimilar metals using fusion welding is generally more challenging than that of similar metals because of the differences in the physical, thermal, electrical, mechanical and metallurgical properties of the parts to be joined [10]. PTA welding has some advantages here such as a high concentration of energy in a small area, giving high welding speeds and producing welds with high penetration/width ratios, thus limiting the HAZ dimensions in materials that are hard to join with dissimilar materials with fusion welding.

In the present study, AISI 430 ferritic stainless steel plate and AISI 1040 carbon steel of 10 mm thickness were butt-welded without any pretreatment using the KPTA technique. The aim of this study was to investigate the weldability of dissimilar materials and the effect of process parameters on the keyhole size, penetration depth, microstructure and mechanical behaviors.

2 Materials and experimental methods

AISI 430 ferritic stainless steel and AISI 1040 steel, both with dimensions of 125×50×10 mm, were welded in the butt position without any pretreatment of welding using the KPTA welding process. The chemical compositions and weight percentages of test materials are listed in Table 1. Welds were produced using plasma welding equipment in which the torch was fixed to an automatic mobile system to control both the travel speed and the nozzle/workpiece distance. Pure argon gas was used as both the shielding gas and the plasma gas. The flow rate of the shielding gas was 20 l/min, the flow rate of the plasma gas was 1.1 l/min and the diameter of the orifice was 2.4 mm. These parameters were the same in all experiments conducted in our study. A schematic representation of the KPTA welding system is shown in Fig. 1, and the process parameters for keyhole welding are given in Table 2. For metallographic examination, the welded specimens were cut transversely through the bond using a low speed saw. The cross-section areas of these joints were metallographically polished using 3 μm of diamond paste as a final polish and then cleaned using acetone. For microstructural examination, the welded specimens were etched in a solution of 2% NHO_3 and 98% alcohol, and specifically, AISI 430 sides were etched electrolytically in a solution of 50% HCl+30% H_2O+20% NHO_3. Scanning Electron Microscopy (SEM), Energy Dispersive Spectrometry (EDS) and X-ray Diffraction (XRD) were used for investigating the microstructures of all specimens. The mechanical performances such as microhardness, tensile strength and impact strength were also tested. Microhardness measurements were performed by a Leica microhardness tester using a typical Vickers tip under a load of 50 g for 15 s. The tensile test specimens were prepared according to TS 138 EN 10002-1 standards (see Fig. 2) [11], and the entire weldment region (weld metal, heat-affected zones [either side] and base materials) was in the gauge sections of both tensile and impact test specimens. A

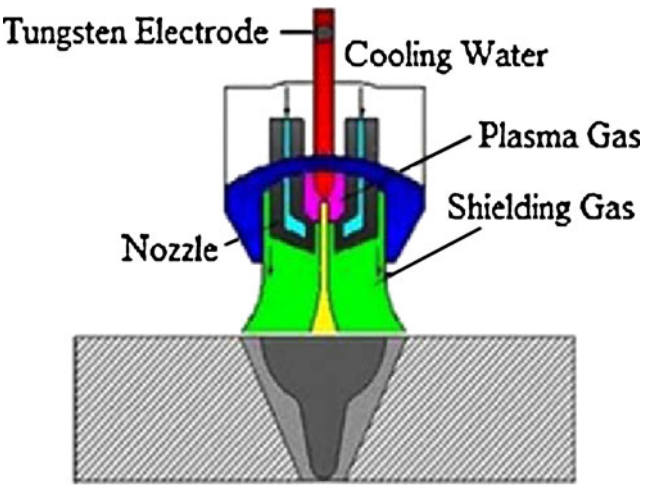

Fig. 1 Schematic presentation of keyhole plasma transfer arc welding system

Table 2 The processes parameters used in KPTA welding of AISI 430 to AISI 1040

Specimen no.	Welding current (A)	Plasma gas flow (l/min)	Shielding gas flow (l/min)	Traverse speed (m/min)	Orifice diameter (mm)	Nozzle/workpiece distance (mm)
S1	130	1.1	25	0.01	2.4	3
S2	130	1.1	25	0.02	2.4	3
S3	130	1.1	25	0.03	2.4	3
S4	135	1.1	25	0.01	2.4	3
S5	135	1.1	25	0.02	2.4	3
S6	135	1.1	25	0.03	2.4	3
S7	140	1.1	25	0.01	2.4	3
S8	140	1.1	25	0.02	2.4	3
S9	140	1.1	25	0.03	2.4	3

schematic diagram for this configuration is shown in Fig. 3. A hardness traverse (survey) was made across the weldment using a Vickers hardness tester under a 2 N load. Tensile tests were performed on a 250 kN servo-hydraulic machine operated in a ram displacement control at room temperature with a nominal strain rate of 0.2 s^{-1}. Impact test specimens were prepared to dimensions of $55\times10\times10$ mm^3 and then the specimens were tested using a Wolpert PW30 V-notch impact test device with a hammer of 300 J.

3 Results and discussion

3.1 Evaluation of macro and microstructure properties

Figure 4a, b and c show the width and top surface of weld metal realized by keyhole PTA process using three different welding currents. As can be seen in the figures, the width of weld metal are approximately 10, 13 and 15 mm for the welding currents of 130, 135 and 140 A, respectively. By the increase of the welding current, obtained higher heat input reasons to a greater increase in the volume of weld metal. Figure 5a, b and c show penetration depths of the specimens joined by KPTA process using different welding speeds and currents. The penetration depths of specimens S1, S4 and S7 were obtained as 6.5, 7 and 10 mm, respectively, (Fig. 5). These results show that welding speed and energy input are noteworthy parameters in keyhole plasma welding. According to our results, the penetration depth of the specimens decreased with the increase of welding speed. The highest penetration depth was obtained for the welded joints S1, S4 and S7 with a plasma gas flow rate of 1.1 l/min and a welding speed of 0.01 m/min. As a matter of fact, it was not possible to achieve a deeper penetration for welded joints produced by applying a welding speed in the range of 0.02 to 0.03 m/min. The weld metal that existed in the interface which was produced using higher heat inputs and lower welding speeds formed a keyhole profile.

Figure 6 depicts the evaluation of the microstructure that occurred at the welding interface (adjacent to the weld zone HAZ-A=AISI 1040 side and HAZ-B=AISI 430 side, weld metal). Figure 7a and b shows an optical image and SEM micrograph of the cross-sectional area, and microstructural changes in the interface of these welded joints which were connected by applying a plasma gas flow rate of 1.1 l/min. Examining the microstructure images taken from the weld interface of the welded joints, the structures that occurred

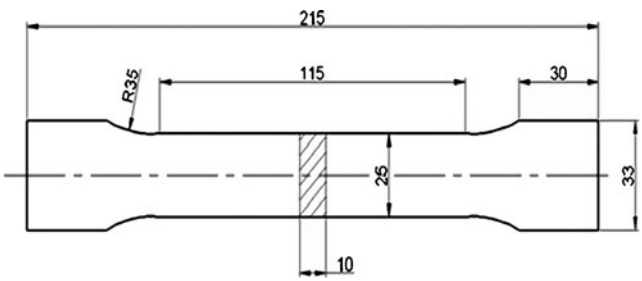

Fig. 2 Dimension of the tensile test specimen

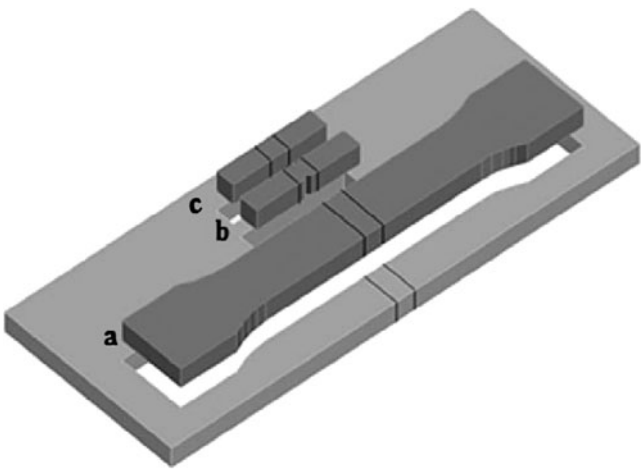

Fig. 3 Scheme of exraction of specimens for mechanical testing. (*a* Tensile test specimen, b impact test specimen, *c* metallographic specimen)

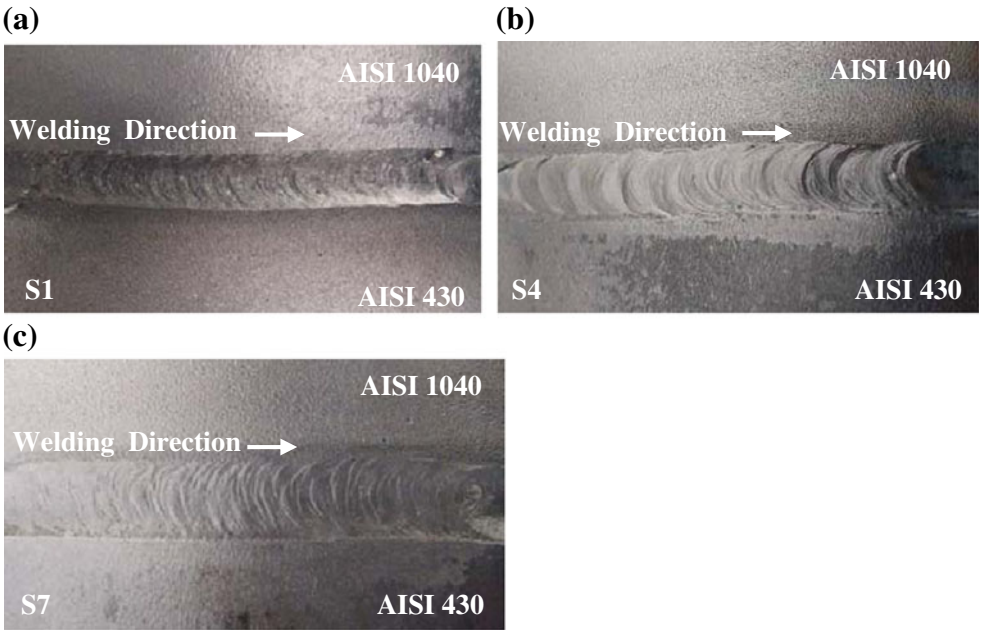

Fig. 4 The surface macroappearance of KPTA-welded specimens. **a** S1, **b** S4 and **c** S7 specimens

were observed to be quite similar, and cracks, cavities and unconnected interfaces were not observed in both transition zones adjacent to the weld zone. On the HAZ-A side, where heat input led to grain coarsening due to its annealing effect, existed plenty acicular ferrite islands and numerous widmanstatten ferrite, lath and plate type martensite. Acicular ferrites were generally formed on the fusion boundary and free surfaces of the material, where the cooling rate was higher. On the HAZ-B side, the zone containing coarse grains which comprised of ferrite phases and chromium carbides, also included intense amount of chromium carbide in specifically intragranular (pepperlike) and grain boundary (lath type) forms as shown in Fig. 7. The effect of the increase in the traverse speed on the microstructure of the HAZ-A and HAZ-B was observed at S3, S6 and S9. As the traverse speed increased, the time needed to reach the maximum temperature decreased and the cooling gradient became steeper due to the heat rapidly absorbed by adjacent region.

Results of XRD analysis for the welded joints S1, S4 and S7 are shown in Fig. 8a, b and c, respectively. From the results of XRD analysis, CrC, $Cr_{23}C_6$, Cr_7C_3 and Cr_3C_2 compounds were seen on the melting zone (weld metal) of welded joints. SEM micrographs and EDS analysis of the welded joint S1 are presented in Fig 9. Point 1 (on AISI 1040 side), point 2 (melting zone), point 3 (weld metal), point 4 (melting zone) and point 5 (on AISI 430 side) are marked as the EDS analysis points. EDS analysis results of specimens S1, S4 and S7 are also given in Table 3. The results of the elemental analysis and microstructural examination in the interface region of welded joints (specimens S1, S4 and S7) clearly demonstrated that different amounts of Fe, Cr, C, Ni, Mn and Si were obtained. Additionally, from the results of EDS analysis taken from weld metal, HAZ-A and HAZ-B for the welded specimens, it was revealed that the partially fused zone had high carbon content and also chrome carbides were precipitated in the form of grain boundary carbides. It was observed that the elemental chrome diffusion occurred towards AISI 1040 carbon steel from AISI 430 ferritic stainless steel, while elemental carbon diffusion took place within the same distance towards AISI 430 steel from AISI 1040 steel as seen in Fig. 9. Since carbon is an interstitial element, as a result they diffused more readily towards the stainless steel. Diffusion of chrome and carbon elements increased depending on the lower welding speed of 0.01 m/min. Increase in welding current intensity and plasma gas flow rate reasoned an increase in the melting point of weld and also in diffusion

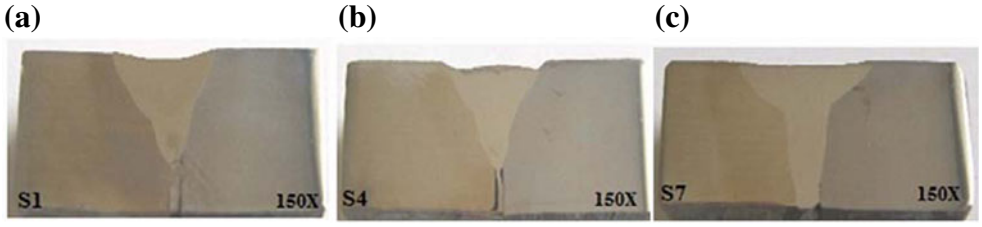

Fig. 5 The cross-sectional macroappearance of KPTA-welded specimens. **a** S1, **b** S4 and **c** S7 specimens

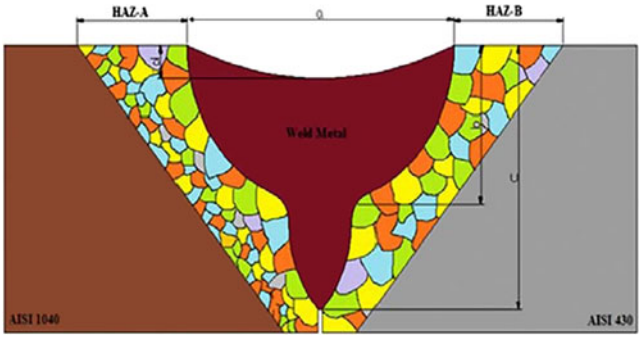

Fig. 6 Schematic representation of the evaluation of the microstructure that occurred in the welding interface

rate. However, a decrease in the diffusion of chrome and carbon elements was observed as the welding speed increased. This can be correlated with the decrease in heat input that is dependent on the increase in the welding traverse speed.

Microhardness measurements in the direction perpendicular to the weld interface of the KPTA-welded joints for specimens S1–S9 are given in Fig. 10a, b and c, respectively. As seen in these figures, a significantly similar trend was observed in the microhardness profiles of all specimens. The hardness of HAZ-A, HAZ-B and melting region increased with a decrease in traverse speed and an increase in energy

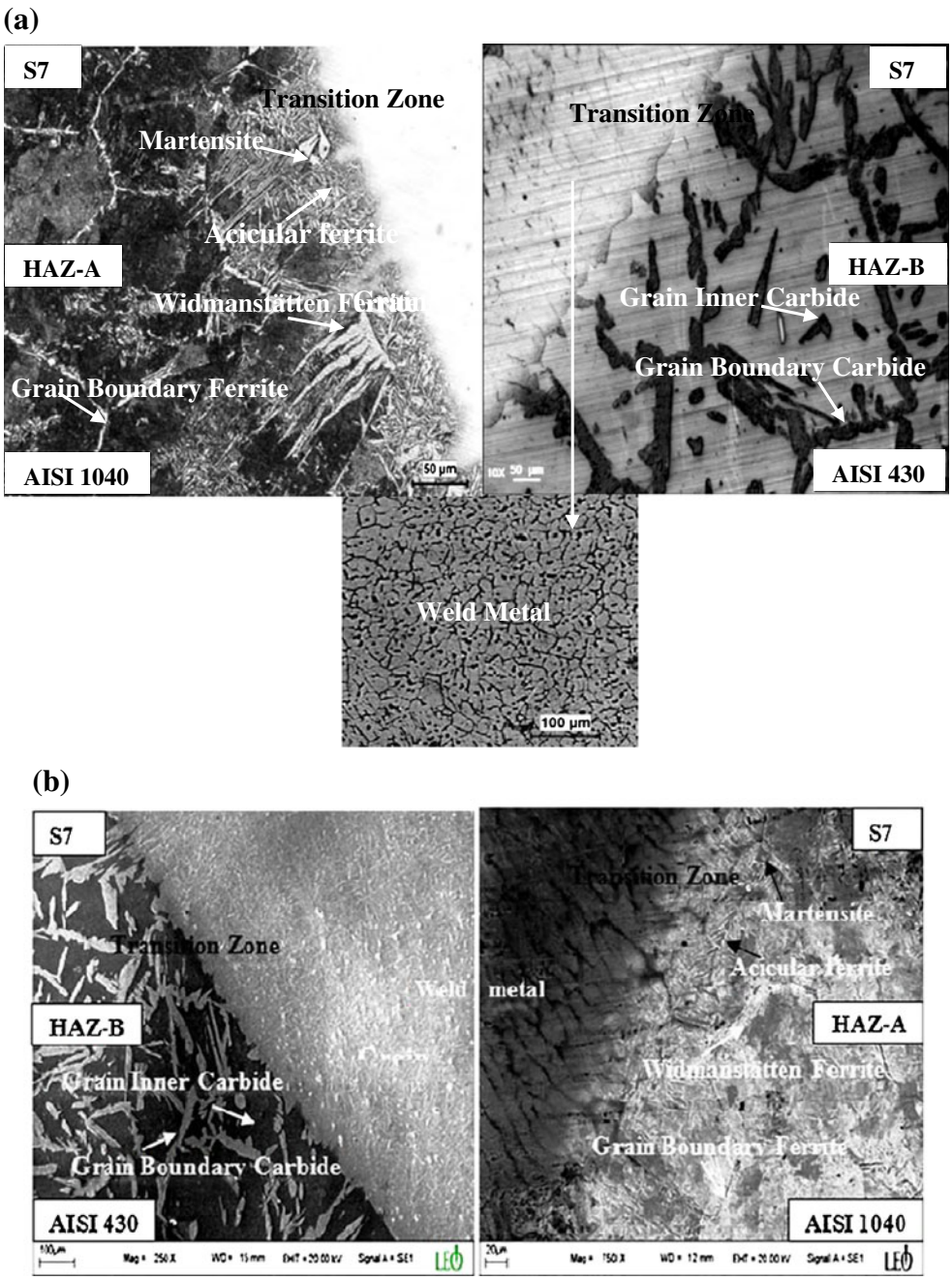

Fig. 7 **a** Optical micrograph taken from the welding interface of S7 specimen. **b** SEM micrograph taken from the welding interface of S7 specimen

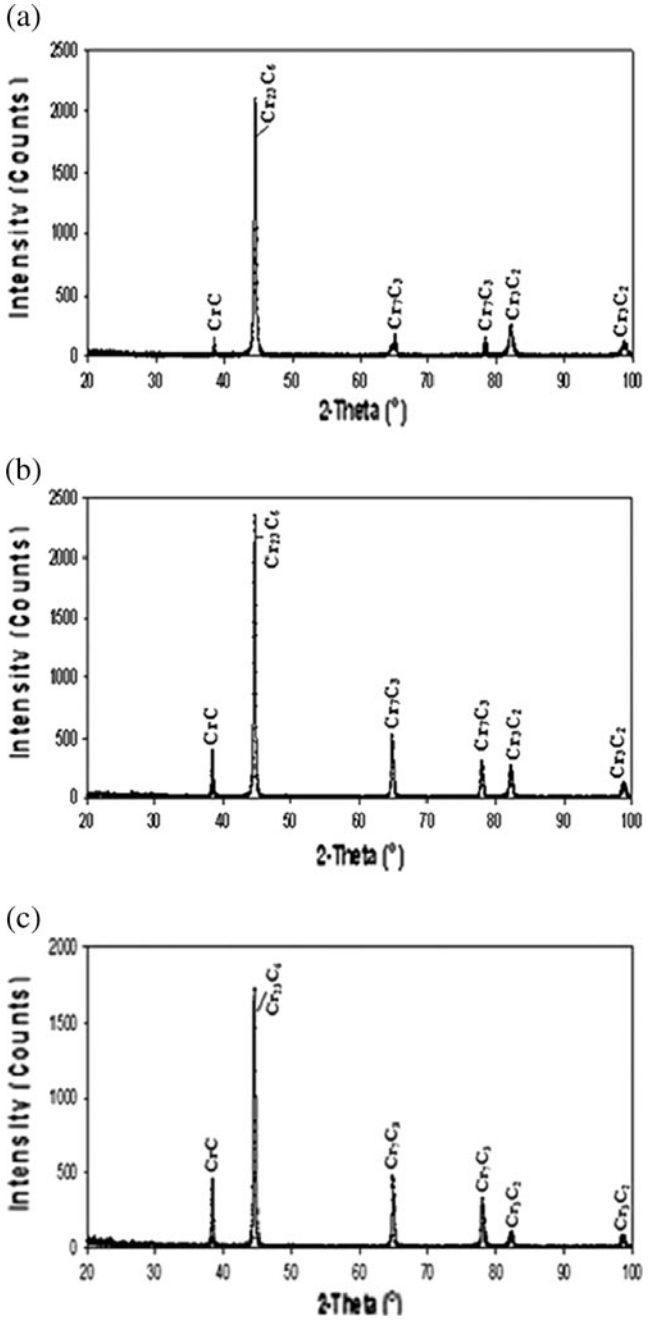

Fig. 8 The results of XRD analyses. **a** S1, **b** S4 and **c** S7 specimens

input. The increase of hardness in the welding interface might be related directly to the microstructure formed in the welding interface. Formation of chrome carbide phases and a martensitic structure in the intermediate zone as a result of rapid cooling increased the hardness across the weld seam zone. Due to this result, higher microhardness values were observed across the weld seam. The highest hardness value achieved in the intermediate zone of weld metal was 515 HV for specimen S7. These higher hardness values for the weld metal were directly related to higher alloy content and lower traverse speed, which resulted in both recrystallized carbides in the microstructure. For these specimens, higher hardness values were reached on the AISI 1040 side by increasing the welding current which can be claimed as the result of higher energy input. In addition, on the AISI 1040 side, a drastic decrease was observed right at the edge of the seam. This zone was carbon depleted and also partially fused. Consequently, in the case of higher heat inputs and cooling rates, the hardness of the welding zone became higher, but the hardness values rose where no carbide formed and there was no effective diffusion of the welding zone due to the formation of martensite rises. From the results of XRD analysis, CrC, $Cr_{23}C_6$, Cr_7C_3 and Cr_3C_2 compounds were observed on the weld metal of these welded joints. With KPTA method ensuring higher energy input, a more uniform distribution of intensive carbide formation and presence of other hard phases in the microstructure positively affected hardness. Furthermore, higher microhardness values were obtained across the weld result from the incomplete dendritic structure formation in small proportions due to rapid cooling. The hardness profile showed a decrease on HAZ-A and HAZ-B zones adjacent to the weld metal, i.e., close to the weld seam. It was considered that the decrease in hardness values across these zones resulted because of the diffusion of carbon on the AISI 1040 side and the diffusion of chrome on the AISI 430 side towards the weld metal, and owing to grain coarsening and concentration gradient, the cause of said zones were being under the influence of heat for an extended period of time depending on the energy input. This change was supported by the elementary concentration profile obtained from the EDS analysis on these zones.

On the AISI 430 side, it was observed that hardness increased slightly at a zone closely adjacent to the weld metal. From the microstructure images, it was understood that the increase in hardness was caused by the grain boundary carbide distribution and formation. Results obtained for all of the weld joints were similar to this structure. The unit area of welded metal would decrease the heat affected time depending on the increase of welding traverse speed. Therefore, it helped to quickly exceed the temperature that was in the undesired chrome carbide formation range during the welding of stainless steels. Based on this fact, the application of lower welding traverse speed to produce the welded joints (S1, S4 and S7) led to lower hardness values across the weld metal.

3.2 Evaluation of mechanical properties

3.2.1 Tensile test

Figure 11 shows the stress–strain diagram of specimens S1, S2 and S3 welded by applying a 130 A current intensity,

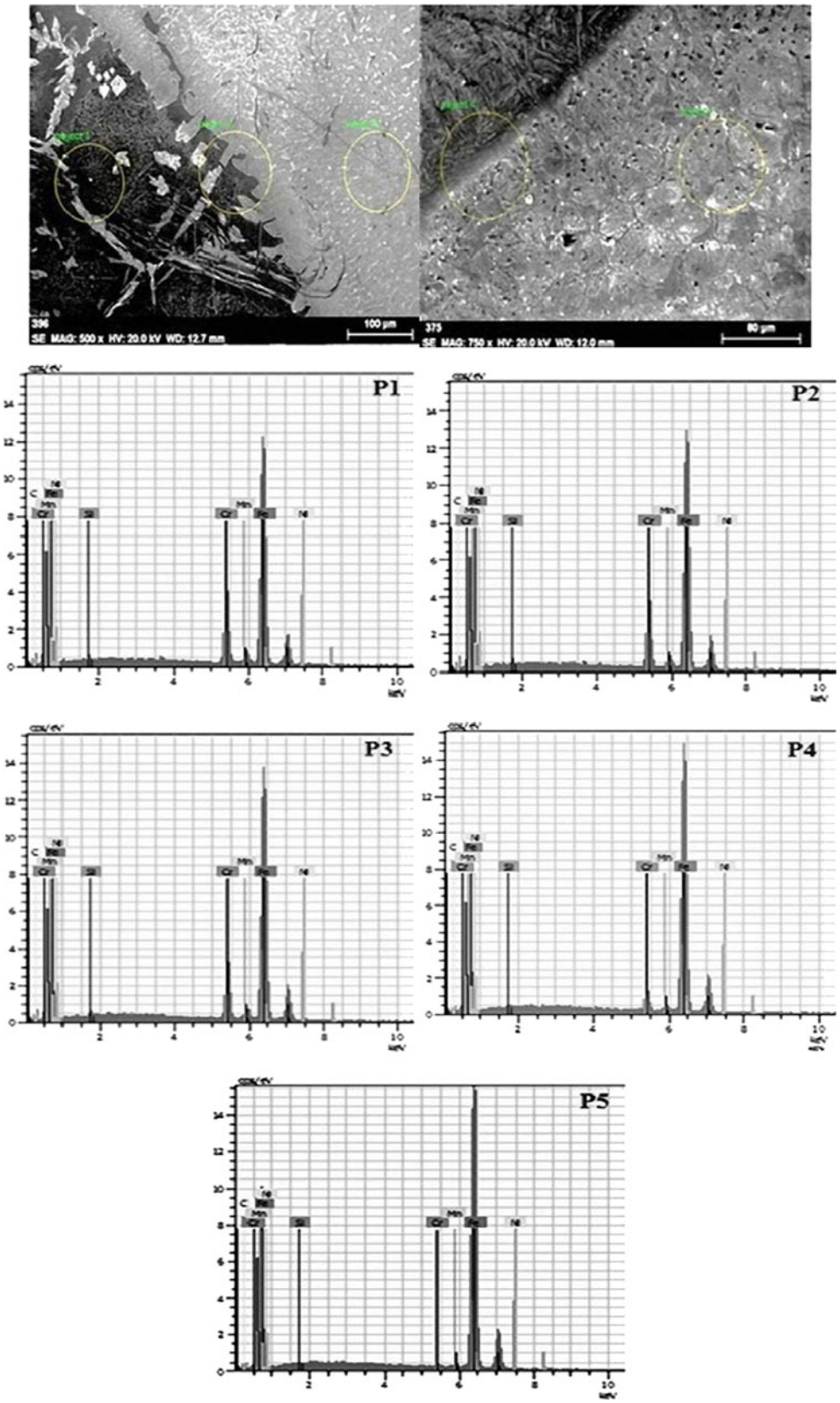

Fig. 9 The SEM micrographs and EDS analyses points across the welding interface of the KPTA-welded specimen S1

three different welding traverse speeds and a constant plasma gas flow rate. Maximum tensile strength values were found to be as follow: S1=304.3 N/mm^2, S2=284.1 N/mm^2 and S3=253.7 N/mm^2. A decrease was observed at the

Table 3 EDS analyses results of S1, S4 and S7 specimens

Specimen no.	Analyses points	EDS analyses (wt.%)					
		C	Si	Cr	Mn	Fe	Ni
S1	1. Point	0.14	0.50	14.58	2.62	79.69	1.13
	2. Point	0.16	0.43	13.76	2.91	80.28	0.95
	3. Point	0.19	0.46	12.83	2.88	81.14	0.75
	4. Point	0.15	0.33	6.35	2.95	88.78	0.86
	5. Point	0.15	0.18	0.57	2.48	95.18	0.90
S4	1. Point	0.28	0.49	14.21	2.81	78.45	1.16
	2. Point	0.22	0.46	12.84	2.93	80.41	1.12
	3. Point	0.10	0.36	8.59	2.77	85.96	1.00
	4. Point	0.14	0.35	6.77	2.69	87.92	0.81
	5. Point	0.13	0.25	0.50	2.77	94.27	0.83
S7	1. Point	0.25	0.39	14.35	3.65	77.89	1.14
	2. Point	0.27	0.51	13.29	2.96	79.46	1.07
	3. Point	0.21	0.59	11.07	3.15	81.97	1.09
	4. Point	0.16	0.34	4.14	2.92	90.01	0.97
	5. Point	0.16	0.26	0.54	2.72	93.84	1.01

tensile stress depending on increase in the welding speed by examining the tensile test diagram obtained. Such a decrease in the maximum tensile stress is directly associated with the penetration depth. Presence of an unconnected section on the interface of two metal pairs created a notch effect and played an important role on the fracture behavior of the tensile test specimens. The fracture occurred on AISI 1040 side for the S1 and S2 specimens. This was influenced by structural changes resulting from the welding of carbon steels by means of fusion welding methods. Examining the interface microstructures of these specimens, there was grain coarsening and lath- and plate-type martensite existed on the HAZ-A after the welding process in the AISI 1040 side. Martensite is known to have a hard and brittle structure. A body-centered crystalline structure does not have hard packaged slip planes on which dislocations can easily move. In addition, if carbon and chrome content is higher, precipitation of the carbide particles not only results in distribution hardening but also causes to brittleness and fragility. All carbides have complex crystal lattices without slip planes and, therefore, they are hard and brittle. As a result, grain coarsening and intergranular carbide precipitations have an adverse impact on the mechanical properties of welded joints. Initially, grain coarsening and precipitations significantly affected the mechanical properties herein, and in the last case, existence and quantity of martensite contributed to the mechanical behavior. Hence, for entirely ferritic microstructures, it appeared that the form of precipitations had an inevitable effect on toughness and ductility; particularly, they had a stronger effect when combined with coarse grain size. Sathiya et al. pointed out in their study that toughness was not only dependent on grain coarsening. They also mentioned that the strength of the welded joints was associated with martensite formation in the HAZ [12]. It was observed that fracture took place along different lines in these specimens which broke without adequate elongation and neck. If two metal pairs with different chemical compositions (AISI 430/AISI 1040) are welded by means of the melting welding method, fracture must occur either on the AISI 1040 side or weld metal. It was seen that the fracture took place in a diagonal manner in specimen S1, on the AISI 1040 side in specimen S2 and in the weld metal in specimen S3. Although, there seemed to be essentially a significant contradiction which was considered as this difference would shorten the period of time during which unit area was being influenced by the energy formation on the nozzle depending on the increase in the welding traverse speed, and therefore, it was caused by lower penetration depths and size of the unconnected sections [13]. All of the ferritic stainless steels solidify like initial ferrite, and therefore, they have relatively rare cracks.

Figure 12 shows the stress–strain diagram of specimens S4, S5 and S6 welded by applying a 135 A current intensity. Maximum tensile strength values were found to be as follows: S4=315.1 N/mm^2, S5=291.5 N/mm^2 and S6=262.3 N/mm^2. It was observed that all the three welded joints showed a brittle fracture behavior without neck. Examining the fracture mechanisms of these specimens, it was seen that fracture took place on the AISI 1040 side in specimen S4 and on the AISI 430 side in specimens S5 and S6. For these welded joints made by increasing the current intensity, the

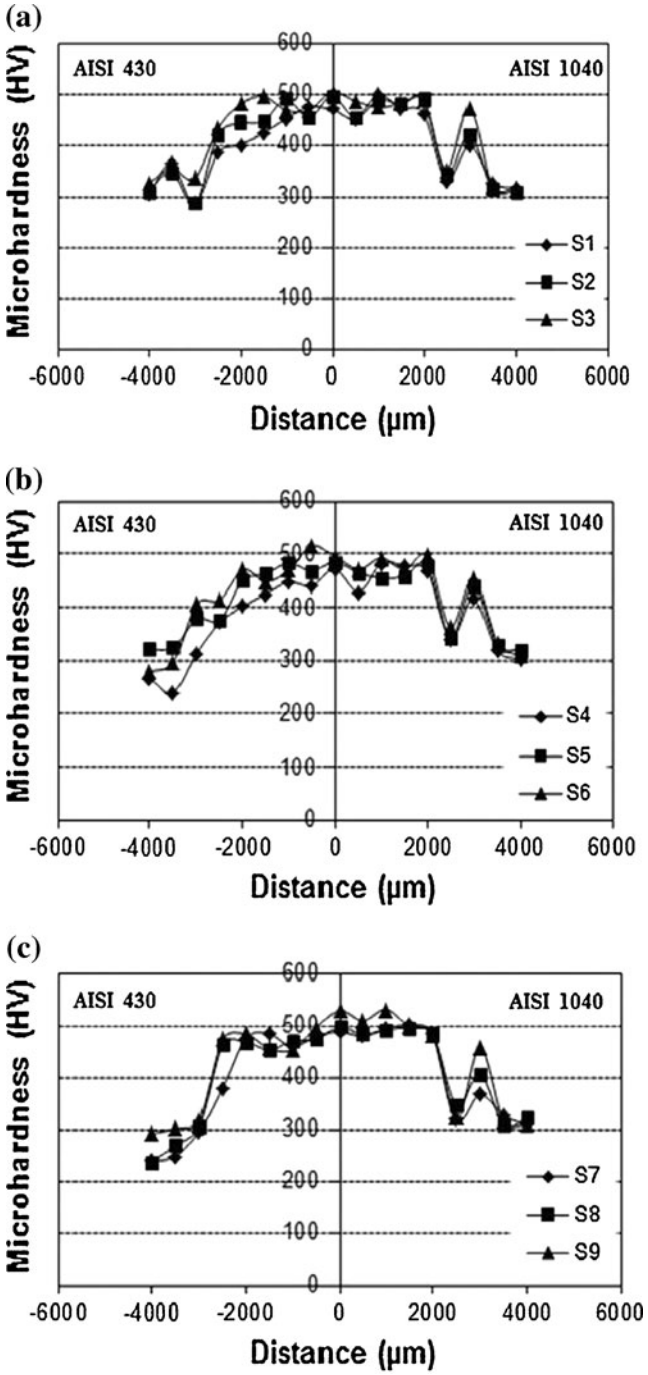

Fig. 10 Microhardness distribution across the welding interface of KPTA-welded specimens. **a** S1–S3, **b** S4–S6 and **c** S7–S9 specimens

resulting tensile strength was somewhat higher than the specimens welded by applying a current intensity of 130 A. This might be attributed to the fact that the penetration depth obtained in the welded joints increased when an increase in the temperature occurred depending on an increase in the current intensity [13].

Figure 13 shows the stress–strain diagram of specimens S7, S8 and S9 welded by applying a 140 A current intensity.

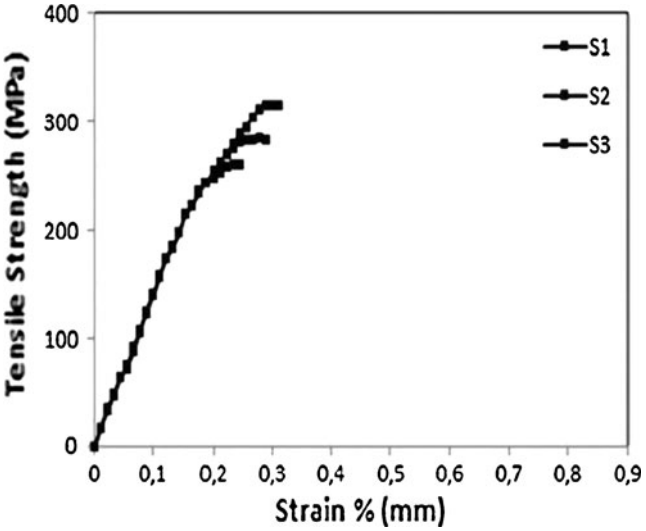

Fig. 11 Tensile test results of specimens S1, S2 and S3

Maximum tensile strength values were determined to be as follows: S7=364.4 N/mm^2, S8=328.5 N/mm^2 and S9=308.3 N/mm^2. Examining the tensile test diagrams of these specimens, it was observed that, depending on the increase in the current intensity, the tensile strength rose because of the cooling process that took place at higher temperatures and the weld metal became more ductile as the cooling rate dropped. However, depending on the increase in the welding traverse speed, the tensile strength decreased and ductility changed less because the heat input gradually reduced [14]. It was seen that fracture occurred on the AISI 1040 side in specimens S7, S9 and on the AISI 430 side of specimen S8.

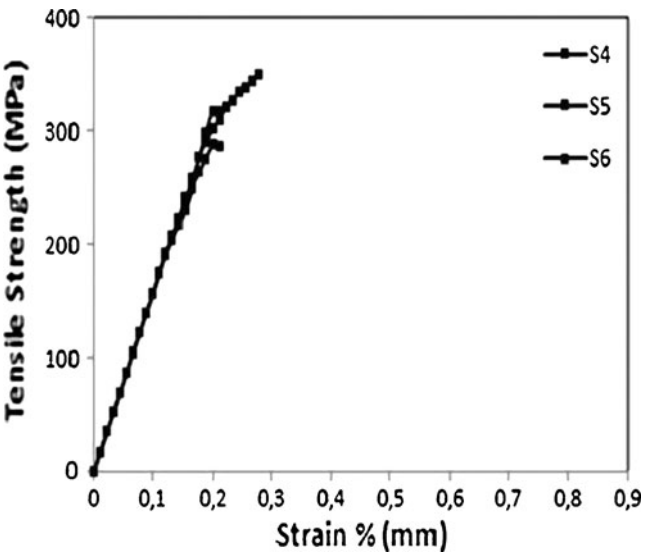

Fig. 12 Tensile test results of specimens S4, S5 and S6

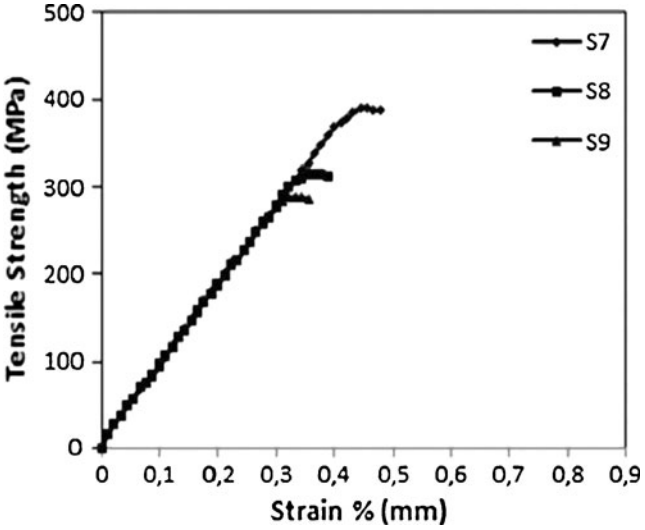

Fig. 13 Tensile test results of specimens S7, S8 and S9

3.2.2 Impact test

Figure 14a, b and c show the results of the V-notch impact test for specimens S1–S9. Examining the notch impact toughness values of the specimens, a decrease of these values was observed depending on the increase in the welding traverse speed. This decrease in the notch impact toughness values was directly associated with the penetration depth, the presence of unconnected zones and structural changes that took place within the joining zone. It is known that the presence and size of an unwelded zone would create a notch effect and have an impact on the fracture behavior of the V-notch impact tests. Therefore, the fracture of the broken specimens occurred on the AISI 1040 side due to the formation of a martensitic structure. Welding traverse speed and plasma gas flow rate had a significant impact on the joining mechanism of the plasma keyhole welding method, too [15]. The period of time during which unit cell was being influenced by the heat would shorten depending on the increase in the welding traverse speed and, consequently, cooling from higher temperatures occurred rapidly. Thus, an undesired hard structure with low toughness inevitably occurred both across the weld metal and the HAZ. In addition, when a pair of two metals with high chrome and carbon contents is welded by means of the melting welding method, the precipitation of chrome carbide particles leads to distribution hardening and causes brittleness. Examining the notch impact test diagrams, the maximum notch impact values were achieved in the specimens welded at the lowest welding traverse speed (S1=10.75, S4=12.25 and S7=18), while a decrease was observed in the notch impact values of specimens (S2=7.60, S3=5.60, S5=9, S6=6.70, S8=14.75 and S9=12.50 J) welded by increasing the welding traverse speed gradually. Concurrently, depending on increasing current intensity, an increase was noticed in the notch impact values of the welded joints. This may be attributed to the fact that the penetration depth increased due to higher temperatures and energy density resulting from increasing current intensity and a rise in heat.

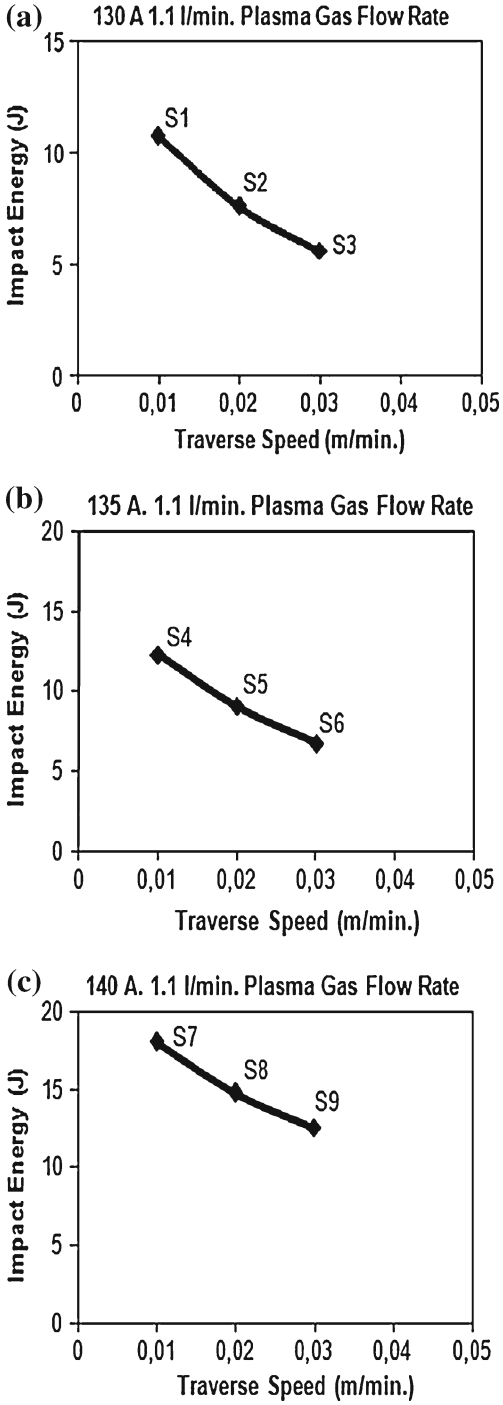

Fig. 14 The notch impact test results of KPTA-welded specimens. **a** S1, S2 and S3; **b** S4, S5 and S6; **c** S7, S8 and S9

3.2.3 Fractography

Figure 15a, b and c shows the images of the fracture surfaces resulting from the tensile test for the KPTA-welded specimens S1, S4 and S7. Examining the fracture surface images, fractures resulting from the tensile test were mostly on the AISI 1040 side, and it was observed that the broken grains had a crystalline fish backed appearance and the specimens displayed a brittle fracture mechanism. For ferritic stainless steels, the fracture morphology was an intergranular crack which was peculiar to brittle fracture, and it was reported that HAZ and the weld metal had excessive grain coarsening. The fracture line stretched across the interface between ferrite and martensite boundaries and along the ferrite boundaries.

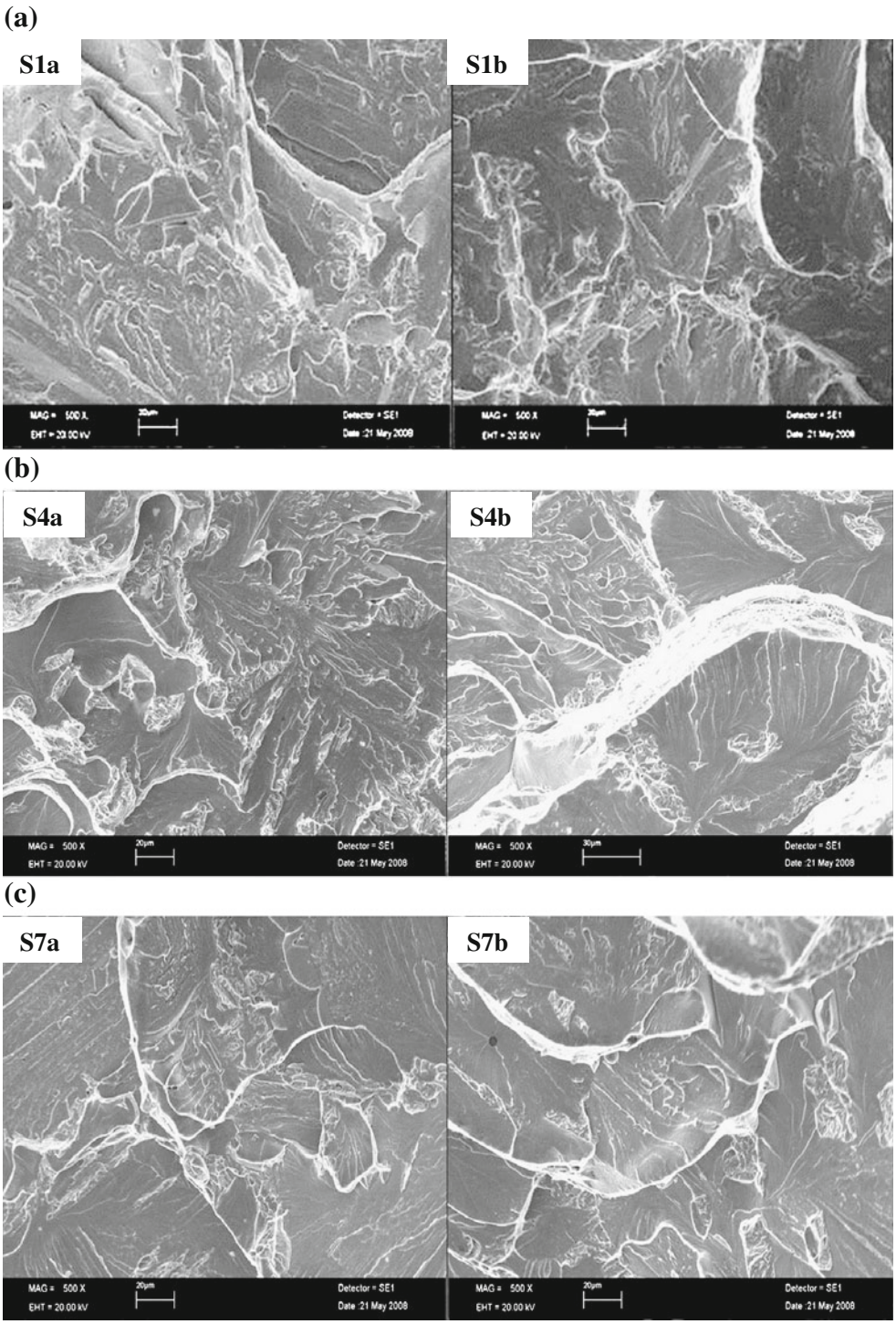

Fig. 15 SEM micrographs of fracture surfaces after tensile test of KPTA-welded specimens. **a** S1, **b** S4 and **c** S7 specimens

4 Conclusions

The following conclusions are made after a thorough investigation of the weldability and joining characteristics of AISI 430/AISI 1040 steel couple using KPTA welding technique:

1. The best penetration depth of joints was successfully produced by KPTA welding technique without any need of using extra welding wire and pretreatment. The significant microstructural changes took place in HAZ-A and HAZ-B regions. The weld width and penetration depth of the weld metal were mainly affected by welding speed and high energy input. Use of a higher energy input and lower welding speed increased the tensile strength of KPTA welded. This infers that the width and formation of the weld metal which, as a result of reaction, took place at the welding interface, have a detrimental effect on the mechanical strength and, consequently, on the parameters of the KPTA welded AISI 430/AISI 1040 steel couple, therefore, need to be controlled.
2. The highest tensile strength and penetration depth were obtained using a welding speed of 0.01 m/min and 140 A of the current intensity applied to the welded specimen S7. Depending on the grain coarsening, a decrease was detected in the tensile strength because of the existence of unconnected sections and the increase in the welding traverse speed. Existence and the size of the unconnected sections on the interface of two metal pairs created a notch effect and, therefore, played a significant role on the fracture behavior of the tensile tests.

Acknowledgements The authors wish to thank University of Fırat Research Fund for their support of this work under the FUBAP-1500 project.

References

1. Raymond T, Slatter E (1998) The plasma advantage in automated welding. Weld J 9:55–57
2. Martikainen J (1995) Conditions for achieving high-quality welds in the plasma-arc keyhole welding of structural steels. J Mater Process Technol 52(1):68–75
3. Vilkas EP (1991) Plasma arc welding of exhaust pipe system components. Weld J 70(4):49–52
4. Irving B (1992) Plasma arc welding takes on the advanced solid rocket motor. Weld J 71:49–50
5. Baeslack B (1993) Welding brazing and soldering. ASM metals handbook, Materials Park, OH 6:605–614
6. Hsu YF, Rubinsky B (1988) Two-dimensional heat transfer study on the keyhole plasma arc welding process. Int J Heat and Mass Trans 31(7):1409–1421
7. Wang Y, Chen Q (2002) On-line quality monitoring in plasma arc welding. J Mater Process Technol 120:270–274
8. Craig E (1988) The plasma arc welding a review. Weld J 67(2):19–25
9. Lesnewich A (1978) In weldability of steels. 3rd ed., Eds. R. D. Stout and W. D. Doty, Welding Research Council, New York, p.5.
10. Lippold JC, Kotecki DJ (2005) Welding metallurgy and weldability of stainless steels. Wiley, Hoboken, New Jersey, pp 88–135
11. TS 138 EN 10002-1 (1996) Metallic materials-tensile testing part 1: method of test (at ambient temperature), (The Institute of Turkish Standards, Ankara, Turkey).
12. Sathiya P, Aravindan S, Noorul Haq A (2007) Effect of friction welding parameters on mechanical and metallurgical properties of ferritic stainless steel. Int J Adv Manuf Technol 31:1076–1082
13. Teker T (2010) Investigation of microstructure and mechanical properties of AISI 1040/AISI 430 steel couple welded by keyhole plasma welding tecnique. University of Fırat, Institute of Natural and Applied Sciences, Ph.D. Thesis, Elazığ, Turkey.
14. Teker T, Ozdemir N (2009) The effect of traverse speed on the mechanical properties of keyhole plasma arc welded AISI 430/AISI 1040 steel. 1st Int Conf on Welding Technol ICWET' 09, Ankara, Turkey, June, University of Gazi, p.p.548-559.
15. Teker T, Ozdemir N (2011) Investigation of microstructure characteristic of AISI 1040/AISI 430 steel couple welded by keyhole plasma arc welding technique. 6th Int Adv Technol IATS' 11, Elazığ, Turkey, May, University of Fırat, p.p.229-234.